*Journal of Applied Fluid Mechanics*, Vol. 17, No. 6, pp. 1230-1242, 2024.
Available online at www.jafmonline.net, ISSN 1735-3572, EISSN 1735-3645.
https://doi.org/10.47176/jafm.17.6.2258

# Numerical Investigation of the Impingement Cooling Characteristics of Sweeping Jets with Phase Change

W. He[1†], A. Adam[1], P. Su[2], H. An[1], D. Han[1] and C. Wang[1]

[1] *Energy Conservation Research Group (ECRG), College of Energy and Power Engineering, Nanjing University of Aeronautics and Astronautics, Nanjing, Jiangsu 210016, China*
[2] *State Key Laboratory of Long-life High-Temperature Materials, Dongfang Electric Group Dongfang Turbine Co., Ltd, 666 Jinshajiang West Road, Deyang 618000, China*

*†Corresponding Author Email: wfhe@nuaa.edu.cn*

## ABSTRACT

This study investigates the cooling features of sweeping jets with phase changes, providing insights into how parameters affect heat transfer. The study aims to improve heat transfer by investigating the cooling effects of a sweeping jet impinging on a concave wall. The Eulerian-Lagrangian particle tracking method was used to examine the impact of Reynolds number, droplet diameter, mist capacity, and impingement distance on heat transfer properties during the sweeping jet impingement cooling. Increasing the Reynolds number from 20,000 to 35,200 results in a 7.1% and 3.3% decrease in average temperature at the axial centerline of the impingement wall, attributed to the cooling effect from droplet phase change. Decreasing droplet diameter from 20 μm to 10 μm reduces temperature amplitude by 11K. At 5% and 7.5% mist ratios, the cooling performance is similar to that of dry air. However, a mist injection of 10% significantly amplifies the cooling effect by 18.8%, providing a more efficient cooling experience. This investigation provides essential perspectives on impingement cooling, offering insights into the impact of various parameters on heat transfer enhancement.

***Article History***

*Received August 27, 2023*
*Revised November 30, 2023*
*Accepted January 11, 2024*
*Available online March 27, 2024*

***Keywords:***

*Sweeping jets*
*Impingement cooling*
*Phase change*
*Water vapor*
*Reynolds number*

## 1. INTRODUCTION

The significance of the oscillating jet cannot be overstated, as it marks a remarkable leap forward in generating spatially oscillating jets without relying on external forces. This unsteady oscillation has broad applications, with notable advantages in the cooling realm. The fluidic oscillator, capable of producing an unsteady oscillating jet, has opened new possibilities in various fields. Its applications extend to crucial areas such as noise control AIAA (2000), separation control Cerretelli and Kirtley (2009), and heat transfer enhancement Camci and Herr (2002). Unlike their steady counterparts, oscillating jets, with their unsteady nature, offer a more uniform heat transfer distribution Agricola et al. (2018).

Furthermore, they can interact with the boundary layer, enhancing local heat transfer rates Schlichting and Gersten (1979) and effectively expanding the impingement region while minimizing collisions Weigand and Spring (2011). In the cooling field, the advantages of oscillating jets become particularly pronounced. The fluidic oscillator, renowned for its self-induction and self-sustaining properties, has gained significant attention in heat transfer enhancement. Initial experimental investigations, such as Thurman et al. (2015) work, examined the impact of fluidic sweeping holes and diffusion-type holes (e.g., generic-shaped 777 holes and square flared holes) on film cooling. Hossain et al. (2018b) further conducted an experimental and numerical study to assess the film cooling performance using fluidic sweeping holes. Their findings revealed the presence of two alternating streamwise vortices in the fluidic sweeping hole across all blowing ratios. These vortex pairs exhibit opposite rotation compared to the conventional counter-rotating vortex pairs observed in the exits of 777-shaped holes, thereby contributing to the lateral dispersion of the film coolant. Subsequent studies by Lundgreen et al. (2017), Park et al. (2018), Kim et al. (2019) and Zhou et al. (2019) have extensively investigated the heat transfer characteristics of a sweeping jet impinging on a flat wall, considering various Reynolds numbers and jet-to-wall spacings. The outcomes demonstrate a significant decline in the heat transfer performance of the total jet as the jet-to-wall spacing increases, owing to the reduction in impinging velocity.

Considerable research efforts have been made to enhance heat transfer by utilizing droplet phase change characteristics. Studies by Li et al. (2001, 2003), Wang et al. (2005), and others have encompassed experimental and numerical investigations of mist/steam phase change cooling in various configurations, including slots, rows, and multiple rows of jets. Khan and Alzahrani (2020) investigated thermal conduction in all phases (liquid, solid, and gas) through the Cattaneo-Christov heat flux model, deviating from the conventional Fourier law. In this analysis, they examine how different flow parameters affect velocity, skin friction coefficient, temperature, and concentration. The findings reveal particle velocity decreases as Deborah number increases, while temperature distribution improves with increased Brownian motion and thermophoresis parameters. Furthermore, depending on the Lewis number and Brownian motion parameter, we observe conflicting effects on concentration. Wang and Dhanasekaran (2010) conducted a numerical simulation of impingement cooling employing mist/steam phase change, which was also experimentally examined by Peng et al. (2009). A comparison of the results with those of single-phase steam impingement cooling revealed a significant augmentation of the cooling effect on the wall due to the heat absorbed during droplet evaporation. Usman et al. (2022) presented a study on Eyring Powell nanofluid's rheological effects and gyrotactic microorganisms' swimming behavior over a Riga plate within a porous medium. Bioconvection fluid flow, influenced by a perpendicularly applied magnetic field, is analyzed considering nonlinear thermal radiation, heat source/sink, and activation energy under convective-field boundary conditions. Khan et al. (2020) and Chu et al. (2020) explored the physical effects of thermo-diffusion and diffusion-thermo on Marangoni convective flow in a hybrid nanofluid, while Song et al. (2021) conducted theoretical investigations on entropy optimization in electro-magneto nonlinear mixed convective second-order slip flow. This study emphasizes the significance of reducing entropy production to improve system heat transfer efficiency. Furthermore, Tan et al. (2013) performed a numerical analysis of the heat transfer characteristics in a mist/air-impinging single-slot jet, exploring the effects of phase-changing heat transfer of water droplets, mist mass ratio in air, and geometrical parameters of the slot jet to elucidate heat transfer enhancement. The findings demonstrated that introducing liquid droplets into an airflow substantially enhances cooling.

While previous research has focused on single-phase sweeping jets for heat transfer enhancement, there is a noticeable gap in the literature regarding investigations into the impingement cooling of two-phase sweeping jets. Mist air, characterized by its excellent aerodynamic and heat transfer properties due to higher specific heat and lower viscosity coefficient, emerges as a promising candidate for enhancing heat transfer. Compared to dry air sweeping jets, mist/air sweeping jets present an efficient technique for enhancing heat transfer.

The current study aims to fill this gap and explore the potential significance of this combination, particularly in applications like blade cooling. To achieve this, the study utilizes the Eulerian-Lagrangian method to numerically simulate the flow field structure and heat transfer of a two-phase sweeping jet impinging on a concave surface. A comparative analysis explores the heat transfer effects of dry air sweeping jets and mist air sweeping jets in impingement cooling, considering parameters such as Reynolds number, droplet diameter, mist mass ratio in the air, and impingement distance. The research contributes essential insights into the complex interplay of these parameters. It provides valuable information for the practical application of sweeping jets in cooling systems, particularly in scenarios involving confined concave walls.

## 2. NUMERICAL INVESTIGATION

### 2.1 Computational Domain and Grid generation

Figure 1 presents a detailed description of the fluidic oscillator design, accompanied by the grid configuration of the computational domain. The computational domain encompasses both the fluidic oscillator and the impact chamber. The fluidic oscillator is composed of a fluidic circuit comprising a power nozzle, a main mixing region, two feedback loops, and a throat or exit aperture. In this study, the radius of curvature is expressed in terms of the throat hydraulic diameter (D = 4.1 mm). The impingement surface, which has a radius of curvature of 20D, is selected

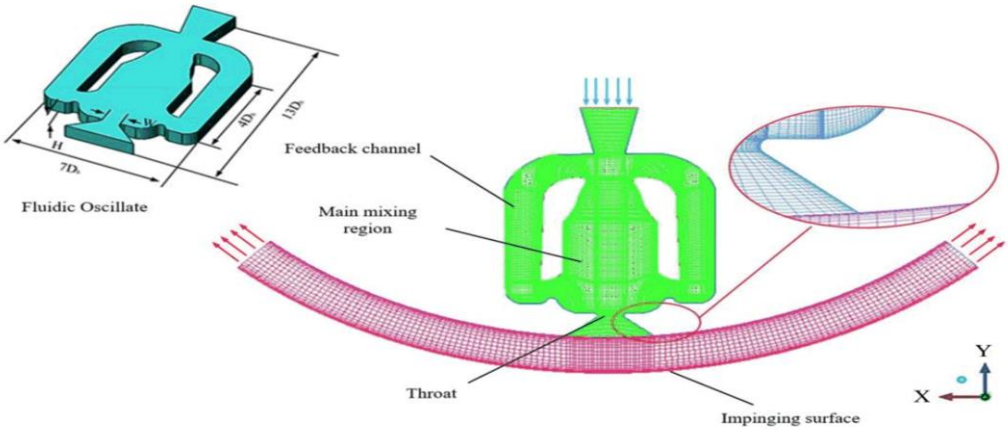


**Fig. 1 Schematic diagram of structured grids with boundary layer encryption and the fluidic oscillator**

as the focal point of the investigation and positioned at a fixed distance of 5D from the jet throat. The coordinate system's origin is situated at the center of the impingement surface, with the Z direction perpendicular to the XY section. Structural grids, consisting of 15 prism layers at the wall, were generated using ANSYS ICEM. The dimensionless wall distance (y+) value is maintained around 1 to capture the significantly larger velocity gradient. These specifications establish the basis for precise simulation and analysis of the heat transfer enhancement of two-phase sweeping jets in impingement cooling applications.

### 2.2 Computational Method

In this study, the simulation of droplet evaporation in mist-air was carried out using Eulerian-Lagrangian trajectory calculations, which enable the modeling of dispersed phases within a continuous phase. The continuous phase in this study is air, while the dispersed phase consists of droplets. To ensure accuracy, the time steps were adjusted between 1.0x10-7 sec to 5.0x10-7 sec, depending on the jet Reynolds number and droplet diameter, in order to maintain a Courant number close to unity. For all sweeping jets, unsteady Reynolds-Averaged Navier-Stokes (RANS) simulations were conducted using ANSYS CFX 19.0, a commercial software, to predict time-averaged flow fields and heat transfer results. The flow equations were discretized using a second-order upwind scheme, and the k − $\omega$ SST model was employed to account for turbulence effects.

### 2.3 Governing Equations

#### 2.3.1. Continuous Phase

The governing equations of mass, momentum, and energy are included in the established equations for the steady state as follows:

Continuity equation

$$\frac{\partial \rho}{\partial t} + \nabla(\rho \vec{u}) = S_{MS} \tag{1}$$

Momentum equation

$$\frac{\partial(\rho \vec{u})}{\partial t} + \nabla \cdot (\rho \vec{u} u) = -\nabla p + \nabla \cdot \tau + \rho \vec{g} + \overrightarrow{F_\sigma} \tag{2}$$

Energy equation

$$\frac{\partial(\rho h_t)}{\partial t} + \nabla \cdot \left(\vec{u}(\rho h_t + p)\right) = \nabla \cdot (\lambda \nabla T) + S_E \tag{3}$$

where $\rho$ is the density, u is the velocity of the continuous phase, p is the static pressure, g is the gravity vector, ht is the total enthalpy of the continuous phase, $\lambda$ is the thermal conductivity, T is the static temperature,

The contribution of the mass source, denoted as " SMS " to the conservation equation for fluid mass is precisely specified, following the same approach as a general source. The source terms (F$\sigma$, SE) is used to include the contributions from the dispersed phase refer to Ansys (2020), $\tau$ is the viscous shear tensor, which is calculated using the following equation:

$$\tau = \mu\left(\nabla \vec{u} + (\nabla \vec{u})^T - \frac{2}{3}\mu \nabla \vec{u} \cdot I\right) \tag{4}$$

where $\mu$ is the fluid dynamic viscosity, and I is the unit tensor.

#### 2.3.2 Turbulence Model

The k-ω turbulence model in the Shear Stress Transport (SST) format was proposed by Menter (1993), which enables independence from the k-ω model in a wide range of fields, thereby enabling k-ω in near-wall free flow. The model achieves a wide range of applications and accuracy.

Turbulent kinetic energy transport equation

$$\frac{\partial \rho k}{\partial t} + \frac{\partial}{\partial x_j}\left[\rho u_j k - (\mu + \sigma_k \mu_t)\right] = \tau_{tij} S_{ij} - \beta^* \rho \omega k \tag{5}$$

Turbulence Ratio Dissipation Equation

$$\frac{\partial \rho \omega}{\partial t} + \frac{\partial}{\partial x_j}\left[\rho u_j \omega - (\mu + \sigma_\omega \mu_t)\frac{\partial \omega}{\partial x_j}\right] = P_\omega - \beta \rho \omega^2 + 2(1 - F_1)\frac{\rho \sigma_\omega}{\omega}\frac{\partial k \partial \omega}{\partial x_j \partial x_j} \tag{6}$$

where, $\rho$ is the density of the fluid; $\mu$is the velocity; $t$ is the time; $x$is the coordinate axis ( $i, j = 1, 2, 3$ , respectively representing three coordinate spaces $x, y, z$ ); $k$ is the turbulent kinetic energy; $\omega$ is the specific dissipation rate.

In the above formula, the eddy viscosity model of Reynolds stress is:

$$\tau_{tij} = 2\mu_t\left(S_{ij} - S_{nn}S_{ij}/3\right) - 2\rho k S_{ij}/3 \tag{7}$$

where, $\mu_t = \rho k/\omega$is the eddy viscosity; $S_{ij}$is the average velocity strain rate tensor; $S_{nn}$is the Kronecker operator; $P_\omega$is the generating term.

$$P_\omega = 2\gamma\rho\left(S_{ij} - \omega S_{nn} S_{ij}/3\right)S_{ij} \tag{8}$$

where, $F_1$ , $\beta, \gamma, \sigma_k$ , $\sigma_\omega$,are all model parameters; $\beta^*$is a model constant, generally taken as 0.09.

#### 2.3.2 Discrete Phase

The motion equation of mist was described in the Lagrangian method with Newton's second law as follows:

$$\frac{d\overrightarrow{u_p}}{dt} = F_D\left(\vec{u} - \overrightarrow{u_p}\right) + \frac{\vec{g}(\rho_p - \rho)}{\rho_p} + \vec{F} \tag{9}$$

where u is the velocity of the continuous phase, $\rho$ is the density of the continuous fluid, up is the particle velocity of mist, $\rho$p is the density of the particle, FD(u − up) is the drag force per unit particle mass, g($\rho$p - $\rho$) is the gravity force per unit particle mass, F is the additional forces.

According to a heat balance equation, the convective heat transfer and latent heat release between the droplet and the continuous fluid are equal to the temperature change in the droplet. The following equation represents the droplet temperature change rate:

$$m_p c_p \frac{dT_p}{dt} = hA_p(T_\infty - T_p) + \frac{dm_p}{dt} h_{fg} \tag{10}$$

where mp is the droplet mass flow rate, cp is the droplet heat capacity, Tp is the droplet temperature, h is the convective heat transfer coefficient, Ap is the droplet surface area, T∞ is the mean temperature of the continuous phase, dmp/dt is the droplet evaporation rate, and $h_{fg}$ is

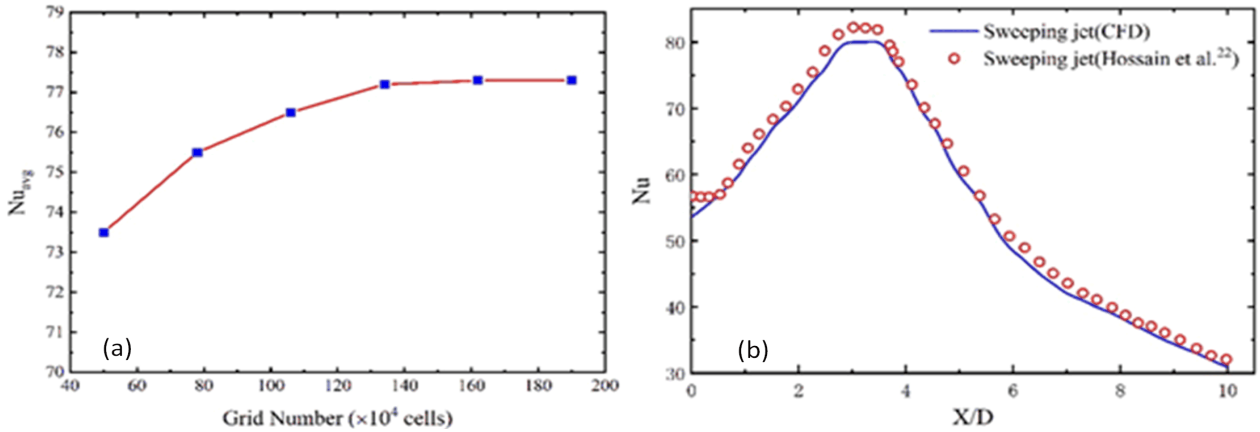


**Fig. 2 (a) Grid Irrelevance Verification, (b) Time-averaged Nu distribution under the same conditions**

the latent heat of the droplets. The empirical correlation generates the convective heat transfer coefficient h:

$$Nu_d = 2 + 0.6\, Re_d^{\frac{1}{2}} \left(\frac{\mu c_p}{k}\right)^{\frac{1}{3}} \quad (11)$$

where Nud is the Nusselt number of the droplet, Red is the droplet Reynolds number; more information can be found in Re f Zhou et al. (2017).

### 2.3.3 Time Average

$$P_{avg} = (\{P\}[1]) + \{P\}[2] + \ldots + \{P\}[n]) / n \quad (12)$$

where P is the required properties, and n is the number of time steps, this equation sums the properties needed in each zone and is divided by the number of time steps. This will become cumbersome for a large number of timesteps and multiple variables.

### 2.4 Boundary Conditions

In this study, the simulation's continuous phase is assumed to be dry air. The inlet conditions are set with a uniform velocity (Vin) and a static temperature (T0). Notably, the inlet velocity ranges from 28.86 to 54.02 m/s, corresponding to throat Reynolds numbers ranging from 20,000 to 35,200. The outlet boundary condition is specified as a static pressure of 1 atm. The boundary conditions of the convection heat transfer coefficient and external temperature are assigned for the sweeping jet impingement wall. The other walls are modeled as adiabatic and no-slip walls, assuming no heat transfer or slip at these surfaces. A turbulence intensity of 5% is prescribed at the mainstream inlet to account for turbulence effects. In the mist cooling simulations, droplets of uniform sizes ranging from 10 to 20μm are considered.

However, it is essential to note that the results should be interpreted as a combination of results obtained for various uniform sizes, as droplet sizes in real conditions are not uniform. The Taylor Analogy Breakup (TAB) model is employed for the secondary breakup models of the discrete phase. Additionally, the particle- particle collision model (PPCM) available in ANSYS CFX accounts for inter-particle collisions and their effects on particle and gas phases. Two different approaches, "reflect" and "trap," are employed to simulate the boundary conditions of droplets at walls. The boundary conditions for the continuous and discrete phases are summarized in Table 1.

**Table 1 Parameters used in simulation for different cases.**

| Zone | Type | Value |
|---|---|---|
| Jet inlet | $T_0$(K) | 450 |
| | $u$(m/s) | 28.86,43.29,54.02 |
| Outlet | $P$(atm) | 1 |
| Impingement distance | $H/D$ | 3,5,8 |
| Impingement wall | $h$(W/m²·K) | 30 |
| | $T_w$(K) | 1600 |
| Droplet size | $d$(μm) | 10,15,20 |
| Mist concentration | $m_t/m_0$(%) | 5,7.5,10 |

## 3. GRID SENSITIVITY AND MODEL VALIDATION

A grid sensitivity analysis was performed using 500,000 meshes to ensure result accuracy. The number of mesh gradually increased until the Nusselt number reached a steady state. The cooling air inlet temperature was 450K, the hot temperature was 1600K, the heat transfer coefficient was 30 w/m2. K, and the Reynolds number was 35200. Figure 2(a) illustrates the investigation of the impingement cooling wall's average Nusselt number ($Nu_{avg}$) under various grid conditions. It was observed that increasing the number of meshes from 500,000 to 1.3 million led to a 3.7 increase in $Nu_{avg}$. The difference between results obtained with 1.3 million and 1.6 million grids was negligible, at only 0.1. Furthermore, the Nusselt number obtained with 1.6 million grids was nearly identical to that obtained with 1.9 million. Considering computational precision and simulation time, 1.6 million grids were chosen for subsequent sweeping impingement cooling geometry simulations.

Figure 2(b) presents the time-averaged Nusselt number along the impingement surface's axial (X) centerline. The trends observed in the time-averaged Nusselt number align with the reference case by Hossain et al. (2018a), as evident from a comparison of the computational data. Although the Nusselt number in the sweeping region (X/D ¡ 3.5) is slightly lower than that in the reference case, the maximum error between the time-averaged Nusselt number obtained in this study and the

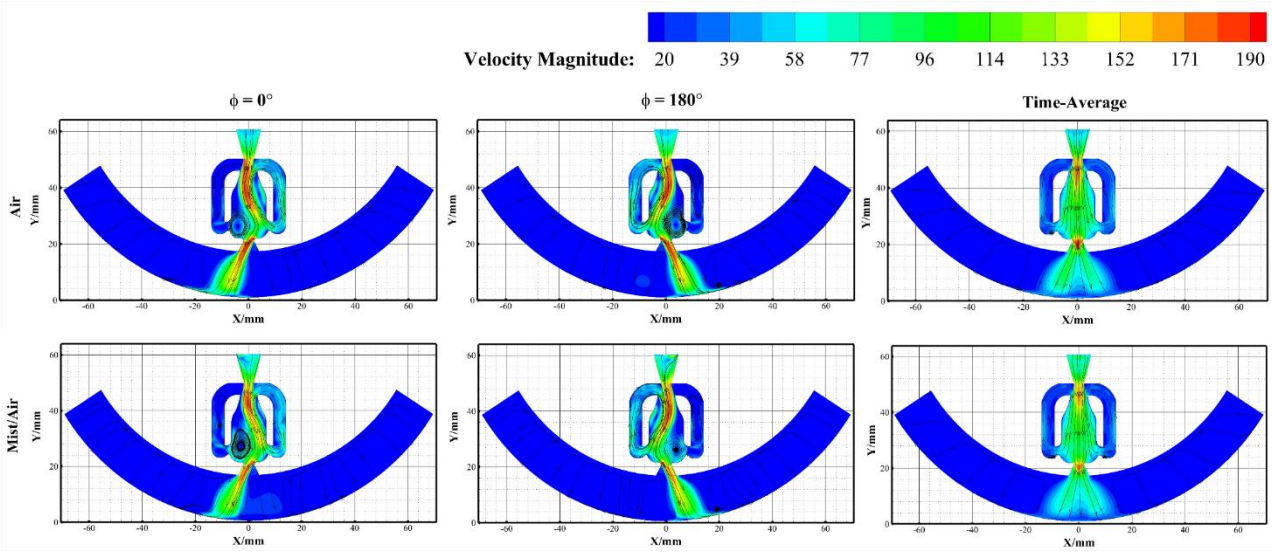


**Fig. 3 Velocity distribution of air and mist/air at the central section**

literature is only 3%. These findings demonstrate that the selected models and parameters are appropriate, enabling a more accurate simulation of the heat and mass transfer processes involved in sweeping jet impingement cooling.

## 4. RESULTS AND DISCUSSION

### 4.1 Analysis of Two-Phase Swept Jet Flow and Heat Transfer Characteristics

The phase angle ($\phi$) is an essential parameter for measuring the periodic oscillation of the swept jet flow. It specifically defines the numerical value of the position of the swept jet flow at any given time. When the swept jet flow is at the leftmost part of the nozzle outlet, $\phi$=0°. To better understand the influence of discrete-phase liquid droplets on the flow field, Fig. 3 compares the velocity distributions of two working fluids at the mid-plane section impacted by the wall under the condition of ReD = 35200 the other physical parameters as in Table 1. Here, $\phi$=180° represents the rightmost position of the swept jet flow, and the Time-Average is the numerical value obtained by calculating the time average of the physical quantities over 10 cycles.

From the figure, it can be observed that the jet stream deviates under the action of vortices in the mixing chamber, moving from the position of $\phi$=0° to$\phi$=180°. During this process, the liquid droplets cause disturbance in the air at the inlet nozzle. This disturbance results in a significant reduction in velocity and varying degrees of curvature in the streamlines. However, the velocity and streamlines in other regions of the impinging structure remain largely unaffected. The time-averaged flow field distribution shows that the sweeping motion of the jet downstream of the throat is not continuous. A low-speed region appears at the center position, indicating that within one sweeping cycle, the jet spends more time near the nozzle outlet than in the central part of the nozzle outlet.

Figure 4 shows a comparison of time-averaged temperature distributions for ReD = 35200 on the impinging wall under different working fluid conditions.

The water mist/air-swept jet flow provides a larger area of impingement cooling within the same temperature range, resulting in effective temperature reduction in the sweeping region compared to the dry air-swept jet flow. This is due to the phase change of water droplets, which requires a significant amount of latent heat of vaporization, and the higher specific heat capacity of the water mist/air coolant compared to dry air, leading to the temperature reduction on the impinging wall.

Figure 5 presents the particle trajectories of water mist/air swept jet flow at three different time steps under the conditions of ReD = 35200 and droplet diameter of 10μm. The particles' color reflects the droplets' average

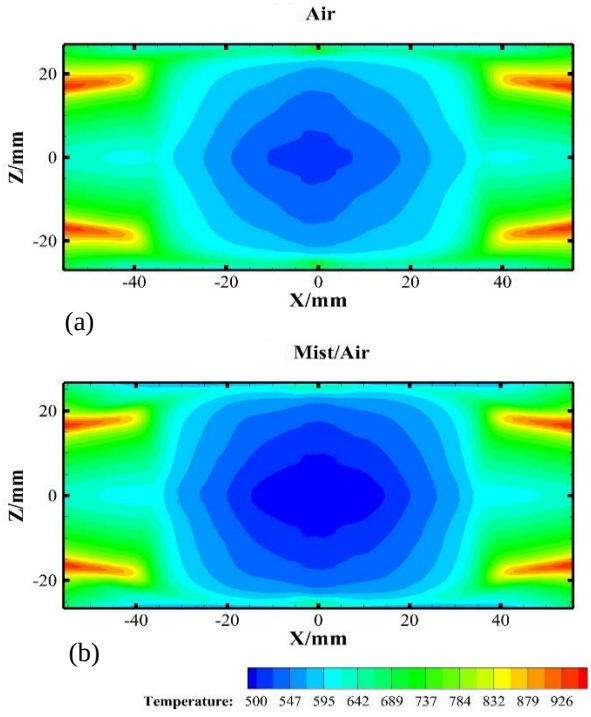


**Fig. 4 Time-averaged temperature distribution of the impingement wall**

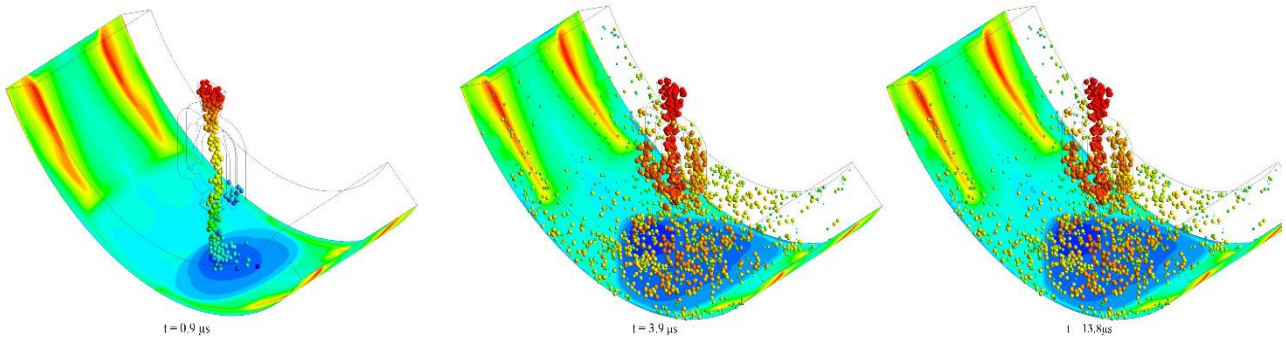


(a) (b) (c)

**Fig. 5 Water droplets motion trajectories**

diameter, while the impingement surface displays the temperature distribution on the impinging wall at the same time step. From Figure (a), it can be observed that a large number of droplets are carried into the impingement chamber. In contrast, a few droplets deviate from the mainstream and enter the feedback channel, indicating good droplet tracking by the airflow and sufficient evaporation within the impingement chamber. Figure (b) shows that the droplet size reduction within the jet oscillator is relatively slow, indicating that most of the droplets in it undergo surface evaporation only, while complete evaporation of droplets occurs within the impingement chamber. Finally, Figure (c) shows that a large number of droplets are carried by the airflow toward the side walls in the impingement chamber, leading to the accumulation of droplets near the sidewalls, which hinders effective droplet evaporation.

**Effect of Changing Reynolds Number on Heat Transfer**

In Fig. 6, the distribution of time-averaged Nusselt numbers is illustrated along the axial centerline of the impinging wall under varying Reynolds number conditions. It is observed that the Nusselt number on the axial centerline increases gradually as the jet's Reynolds number increases. In particular, when the jet's Reynolds number increases from 20,000 to 35,200, the time-averaged Nusselt number on the transverse centerline of the impinging wall experiences a maximum enhancement of up to 96%. However, it is essential to note that the Nusselt number at the impingement center does not reach a minimum value. This discrepancy can be attributed to the absence of bimodal behavior in the oscillating jet when the impingement distance is small.

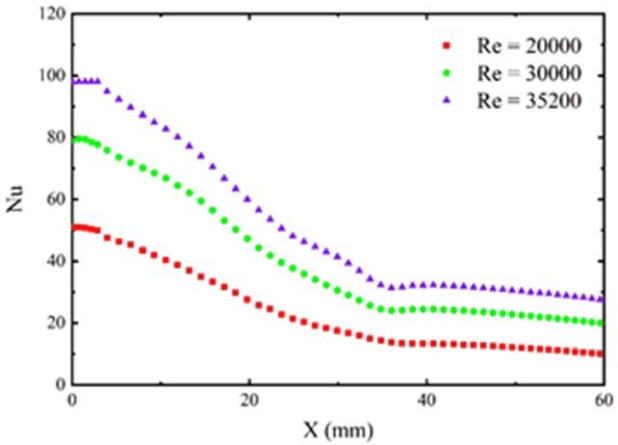


**Fig. 6 Distribution curves of time-averaged Nusselt numbers along the axial centerline of the impinging wall under different Reynolds number conditions**

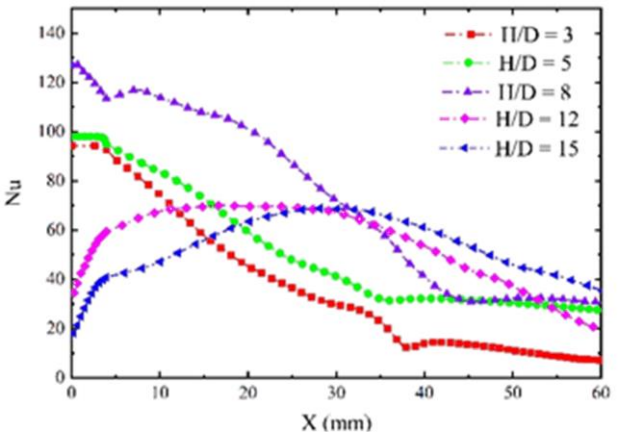


**Fig. 7 The influence of impingement distance on the time-averaged Nusselt number along the axial centerline of the impinging wall**

## 4.2 Effect of Changing Impingement Distance on the Heat Transfer

Figure 7 presents the graphical representation of the time-averaged Nusselt numbers distributed along the axial centerline of the impingement wall under various impingement distances while maintaining a Reynolds number at 35,200. The apex of the Nusselt number at the impingement center is observed when the impingement distance, denoted as the ratio H/D, is 8. A notable enhancement of 35% is detected in the Nusselt number at the impingement center as the impingement distance elevates from H/D = 3 to H/D = 8. However, there is a significant decrease of 605% in the Nusselt number at the impingement center when the impingement distance expands further from H/D = 8 to H/D = 15.

The Nusselt number along the transverse centerline exhibits a unimodal behavior when the impingement distance is set at H/D = 3 and H/D = 5. Interestingly, at H/D = 8, the Nusselt number demonstrates a bimodalbehavior, with the peaks being more centralized than those observed at H/D = 12 and H/D = 15.

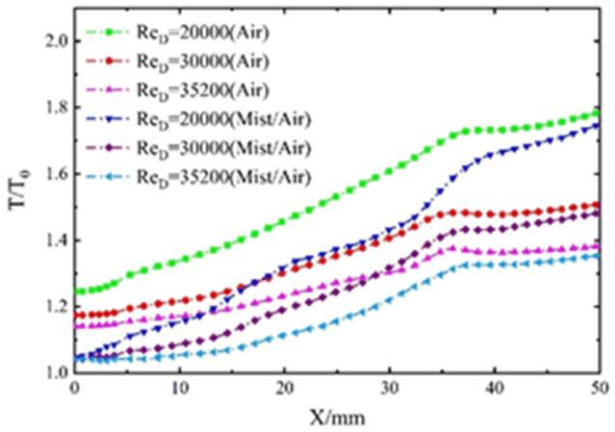


**Fig. 8 Axial midline temperature distribution of impingement wall under different Reynolds numbers**

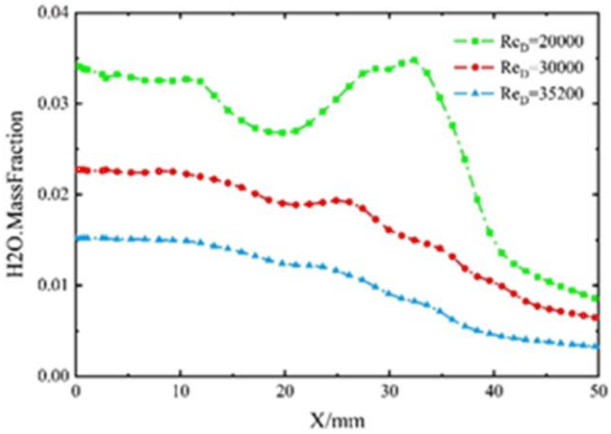


**Fig. 9 Mass Fraction of water vapor on the axial midline of the impingement wall under different Reynolds numbers**

When the impingement distance is small, a circular vortex is formed in the downstream area of the impinging cavity. This causes the airflow that absorbs heat from the wall to recirculate and mix with cooler air from the upper part of the impinging wall. As a result, the overall air temperature within the cavity increases, making it harder for the airflow to absorb more heat from the wall.

### 4.3 Effect of Changing Reynolds Number on Phase-Change Heat Transfer

Figure 8 depicts the dimensionless time-averaged temperature distribution curves for air and mist-air sweeping jets as they impinge on the wall along the axial centerline under varying Reynolds number conditions. Owing to the symmetry of the whole jet impingement model structure, only the portion of the impingement centerline on the right side (X > 0) is represented. In investigating the Reynolds number's influence on the cooling effect, the droplet diameter, the humidification capacity, and the impingement distance are set at 10μm, 5.0%, and H/D = 5, respectively.

In the case of air impingement cooling, the mean temperature along the axial centerline of the impingement wall decreases from 703K to 617K and 575K, respectively, as the Reynolds number escalates from 20,000 to 30,000 and 35,200. This signifies a temperature reduction of 13.9 and 22.3 percent, respectively. The decrement in the impingement wall's temperature with the increasing Reynolds number aligns with the results reported by Kim et al. (2019).

For mist-air impingement cooling, the time-averaged temperature along the axial centerline of the impingement wall surface decreases from 653K to 582K and 556K, respectively, as the Reynolds number increases from 20,000 to 30,000 and 35,200. This correlates to a temperature reduction of 12.2 and 17.4 percent, respectively. The cooling effect on the impingement wall is less influenced by the Reynolds number in mist-air cooling than in air cooling, and the temperature at the impingement center (X = 0) does not diminish with an increasing Reynolds number. Two primary reasons can explain this. Firstly, as the Reynolds number increases, the number of droplets following the jet into the impingement chamber and the height of the liquid layer on the impingement surface rise, thereby causing the surface heat transfer coefficient to be less impacted by the Reynolds number. Secondly, the droplet evaporation capacity per unit of time declines, leading to a smaller temperature gradient between the droplet and the impingement surface, thereby mitigating the impingement wall's heat transfer capacity.

Upon comparing the impact of two working substances on the cooling effect of the impingement wall, it can be inferred that the temperature of the impingement wall is lower in mist-air jet cooling than in air jet cooling. As the Reynolds number increases from 20,000 to 35,200, the time-averaged temperature on the axial centerline of the impingement wall decreases from 703K and 575K to 653K and 556K, respectively. This indicates a temperature reduction of 7.1 and 3.3 percent, respectively. Therefore, mist/air impingement cooling can result in superior heat transfer under low Reynolds number conditions. This finding is significant as it can contribute to the development of more efficient cooling systems in various industrial applications.

In this investigation, Fig. 9 delineates the distribution curves of the water vapor mass fraction along the axial centerline of the impingement wall under varying Reynolds number conditions. It becomes clear that the water vapor mass fraction of the impingement wall considerably diminishes with an increasing Reynolds number. This phenomenon can be ascribed to the elevated airflow velocity, which enhances the transportation of droplets and droplet flow velocity, resulting in decreased adequate evaporation time and evaporation capacity of the droplets.

Significantly, when ReD = 20000, the water vapor mass fraction peaks at X = 32 mm, implying that many droplets re-evaporate beneath the jet's sweeping regions. This can be attributed to the low jet kinetic energy, inducing fewer disturbances to the droplets downstream of the sweeping region. Furthermore, many droplets, which are not part of the mainstream, move downstream after the mainstream is deflected, leading to substantial evaporation

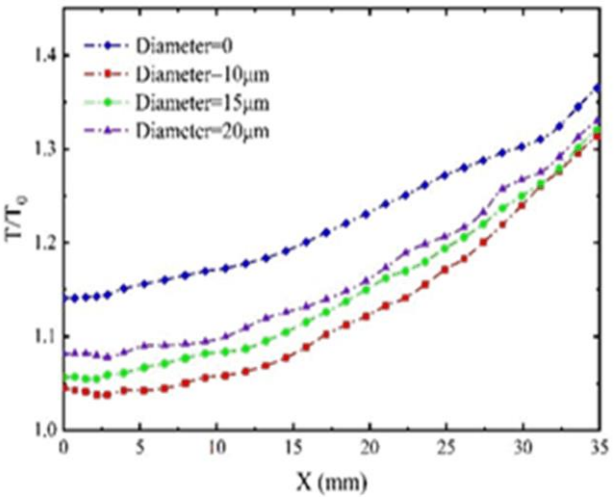


**Fig. 10 Axial midline temperature distribution on the impingement wall under different droplet diameters**

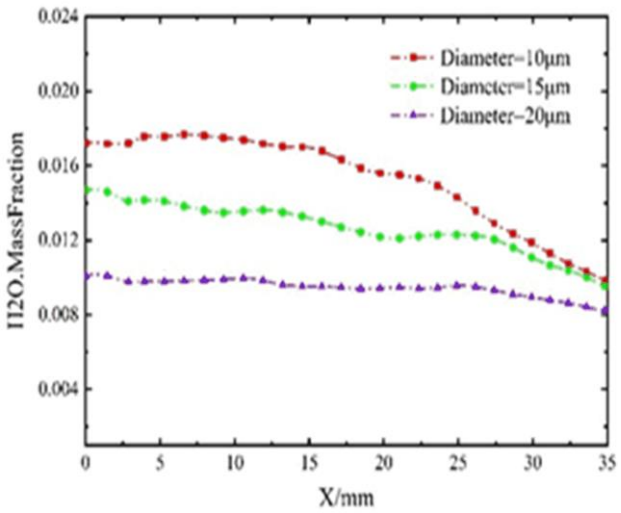


**Fig. 11 Mass Fraction of water vapor on the axial midline of the impingement wall under different droplet diameters**

of droplets, with the maximum concentration observed at X = 32 mm.

### 4.4 Effect of Changing Droplet Size on the Phase-Change Heat Transfer

In practical engineering scenarios, droplets are commonly produced under high pressure through an atomization nozzle, rendering the atomization process relatively intricate. This study analyzes the effects of oscillating jet impingement cooling on forming atomized droplets of varied diameters. Three distinct droplet diameters were selected for analysis to assess the influence of droplet diameter on the cooling of the impingement wall. The Reynolds number was 35,200, the humidification capacity to 5.0%, and the impingement distance to H/D = 5.

Figure 10 showcases the dimensionless time-averaged temperature distribution curves along the axial centerline direction of the impingement wall for different droplet diameters. The time-averaged temperature descends from 570K to 563K and 559K, respectively, as the droplet diameter contracts from 20μm to 15μm and 10μm. The temperature reduction is 1.2% and 2.0%, respectively. These results suggest that as the droplet diameter shrinks, the temperature of the impingement wall decreases. Still, this effect essentially levels off in the downstream region of the impingement wall (X > 32mm). This indicates that smaller droplet diameters of mist-air sweeping jets enhance heat transfer in the sweeping region but not in the downstream region. This phenomenon arises because the sweeping jet compels many droplets to move laterally post- impingement on the wall, accumulating droplets near the front and back walls. At the same time, the return flow impacts the downstream region, causing a drastic reduction in droplet quantity.

Figure 11 presents the distribution curves of the water vapor mass fraction on the axial centerline of the impingement wall under various droplet diameter conditions. The findings illustrate that the evaporation volume escalates as the droplet diameter diminishes. This phenomenon emerges because smaller droplets can evaporate more effectively, which is credited to the more considerable Gibbs free energy associated with smaller droplet diameters. For example, the average water vapor mass fraction on the lateral centerline of the impingement wall increased from 0.007 to 0.009 and 0.011, respectively, as the droplet diameter reduced from 20μm to 15μm and 10μm. This equates to an increase in the water vapor mass fraction by 28.6% and 57.1%, respectively. Likewise, the water vapor mass fraction at the impingement center rose from 0.010 to 0.015 and 0.017, respectively, showing an increase in the water vapor mass fraction by 50.0% and 70.0%.

Figure 12 shows the time-averaged water vapor content distribution and temperature on the impinging wall under different droplet diameter conditions when the Reynolds number is ReD = 35200. The water vapor content distribution indicates that the water vapor content in the sweeping region of the impinging wall (−20 < X < 20) decreases with an increase in droplet diameter. For instance, as the droplet diameter increases from 10μm to 15μm and 20μm, the water vapor content in the sweeping region of the impinging wall decreases by 28% and 50%, respectively. This suggests that smaller droplet diameters have a better cooling effect on the sweeping region of the impinging wall. On the other hand, the temperature distribution shows an opposite trend to the droplet diameter. As the droplet diameter increases, the temperature range below 520K in the sweeping region becomes smaller. However, larger droplet diameters have a better cooling effect on the high-temperature region of the impinging wall. The temperature range above 975K decreases with the increase in droplet diameter. Therefore, it is essential to consider the distribution of droplet diameters when considering phase change impingement cooling of an oscillating jet. A distribution with a single diameter is not the most suitable choice for curved surface impingement cooling. Furthermore, when the droplet diameter increases from 10μm to 15μm and 20μm, the lowest temperature on the impinging wall rises by 2.8% and 4.3%, respectively.

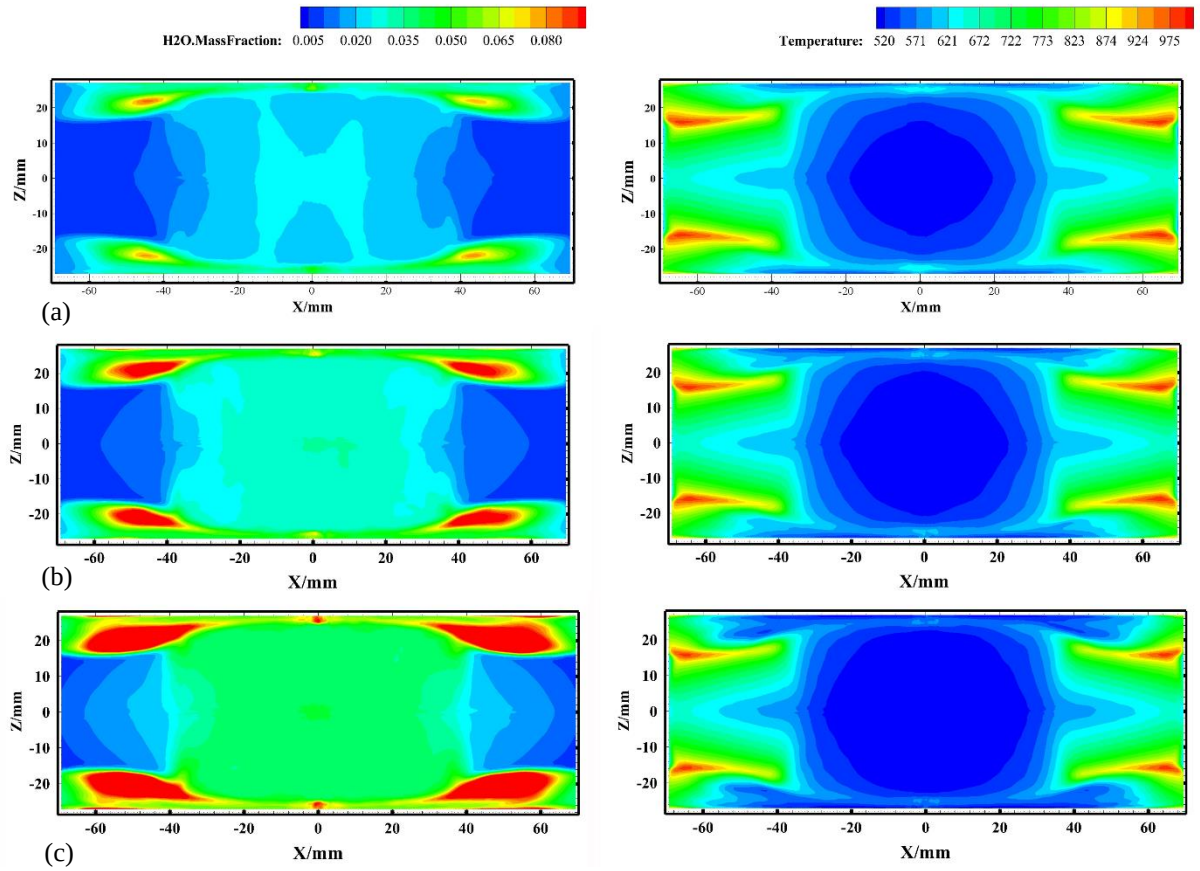


**Fig. 12 The influence of droplet diameter on the time-averaged water vapor content and temperature on the impinging wall: (a)Diameter = 10μm; (b) Diameter = 1μm; (c) Diameter = 20μm**

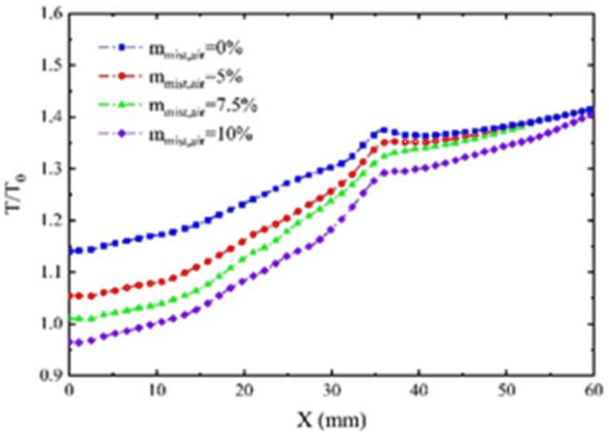


**Fig. 13 Axial midline temperature distribution of the impingement wall under different humidifying capacities**

### 4.5 Effect of Changing Humidification Capacity on the Phase-Change Heat Transfer

The humidification capacity of mist/air, which is defined as the proportion of the mass flow rate of the inlet droplet phase to the overall mass flow rate, is a pivotal parameter in phase change cooling. This study scrutinizes the influence of varying humidification capacities (5.0%, 7.5%, and 10%) on the heat transfer of the impingement wall, employing an impingement distance of H/D = 5, a Reynolds number of ReD = 35,200, and a droplet diameter of 10μm.

Figure 13 exhibits the dimensionless time-averaged temperature distribution curves along the axial center- line of the impingement wall under different humidification capacity conditions. The apex cooling effect was observed at the impingement center, with temperature reductions of 8.5%, 12.8%, and 18.8% as the humidification capacity ascended from 0 to 5.0%, 7.5%, and 10.0%, respectively. As the humidification capacity expanded, the cooling effect gradually converged towards that of air for X > 40mm, owing to the secondary flow that forms after the sweeping jet collides with the target surface. This flow propels the droplets to the front and back walls, resulting in diminished water vapor evaporation in the downstream region and attenuated heat transfer effects for lower humidification capacities.

Figure 14 delineates the time-averaged water vapor mass fraction distribution on the axial centerline of the impingement wall for different humidification capacity conditions. With the escalation in humidification capacity from 5.0% to 7.5% and 10%, the mass fraction of water vapor at the impingement center rose by 48% and 99%, respectively. The water vapor mass fraction at the impingement center exhibits an almost linear surge with the increase in humidification quantity. At X >40mm, the rise in humidification quantity from 5.0% to 7.5% and 10% resulted in a 64.0% and 277.1% upswing in the water vapor mass fraction, respectively. Comparing the graph,

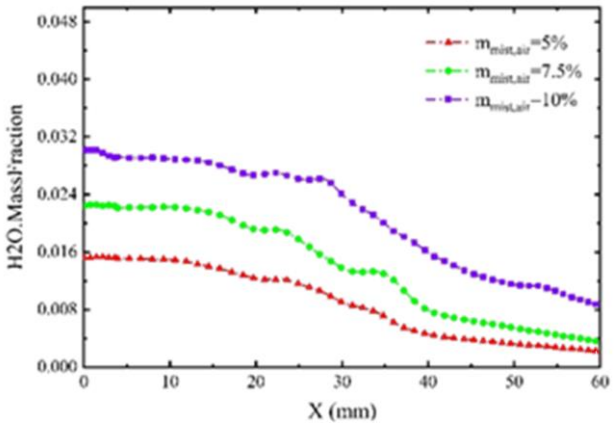


**Fig. 14 Mass Fraction of water vapor on the axial mid-line of the impingement wall under different humidifying capacities**

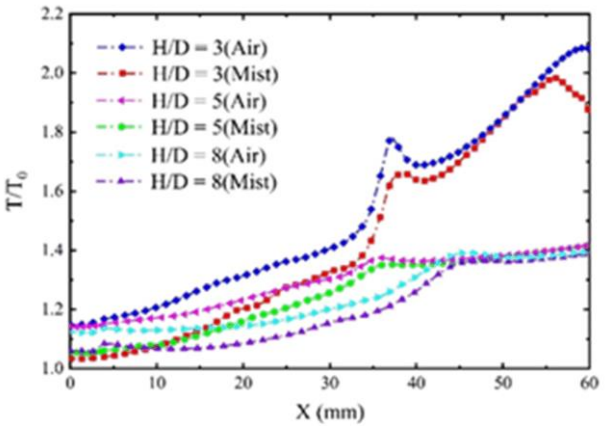


**Fig. 15 Axial midline temperature distribution of the impingement wall under different impinging distances**

it's clear that with a humidification capacity of 10%, more droplets are deviating from the sweeping jet towards the outlet direction, thus facilitating improved evaporation of droplets in the downstream region of the wall.

### 4.6 Effect of Changing Impingement Distance on the Phase-Change Heat Transfer

The cooling effect in impingement cooling mainly depends on the impingement distance. To assess the impact of impingement distance on temperature change along the axial center line, this study conducted experiments under three different impingement distance conditions. The experiments were conducted at a Reynolds number of 35,200, with a droplet size of 10μm and a humidification capacity of 5.0 percent. Figure 15 illustrates the dimensionless time-averaged temperature distribution curves on the axial centerline of the impingement wall for each of the varying impingement distance conditions.

Comparing the effect of the working fluid under the same impingement distance conditions, the temperature at the impingement center was reduced by 11.1 percent due to the development of mist/air cooling with the impingement distance H/D = 3, thereby yielding the highest cooling effect among the other three impingement

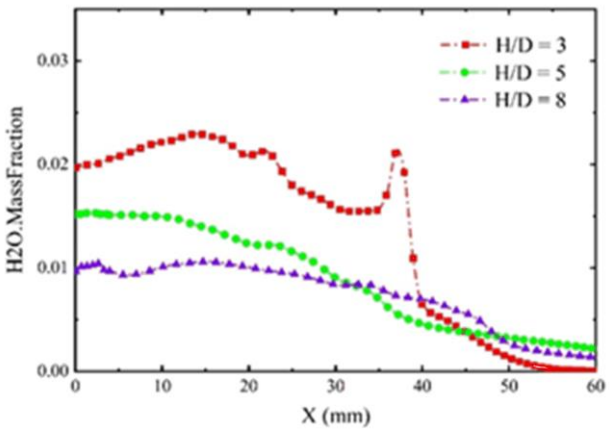


**Fig. 16 Mass Fraction of water vapor on the axial midline of the impingement wall under different impinging distances**

distances. However, the cooling effect of mist-air cooling is effective only in the range of X < 8 with the impingement distance H/D = 3. Beyond X >8, the heat transfer effect markedly deteriorates due to forming of a circular vortex in the downstream region of the impingement chamber. As a result, the back-flow of the airflow absorbs heat from the walls and blends with the cooling air on the upper side of the impingement wall, raising the overall air temperature in the impingement chamber. Consequently, the ability of the airflow to extract more heat from the walls dwindles when the impingement distance is small.

Comparing the cooling effects of air and mist/air, the temperature reduction of the impingement center attributed to phase change cooling is 8.0 percent at the impingement distance H/D = 5. Nonetheless, the cooling effect of mist-air worsens with an expanding lateral distance, and for X > 50, the heat transfer effect is almost indistinguishable from that of air impingement cooling. Mist-air phase change cooling with the impingement distance H/D = 8 decreased the temperature at the impingement center by 5.0 percent. Nevertheless, the phase change cooling effect in the impingement center region (X < 20) is significantly less than that at impingement distances H/D of 3 and 5, despite the mist-air reducing the wall temperature over the lateral range.

Figure 16 shows the time-averaged water vapor mass fraction distribution curves on the axial centerline of the impingement wall under different impingement distance conditions. For example, with an impingement distance of H/D = 3, the water vapor mass fraction on the lateral centerline showcases three peaks. The first peak arises from the jet collision on the impingement center region (X > 0 and X < 15), where a higher wall temperature prompts more droplet evaporation. The second peak stems from the formation of inward-entraining vortices at X = 20, leading to an increased water vapor mass fraction in this region. The third peak arises due to the back-flow at the outlet, resulting in a rapid decline in the mass fraction of water vapor in that area. As the impingement distance increases, the effect of back-flow on the mass fraction of water vapor near the inlet diminishes.

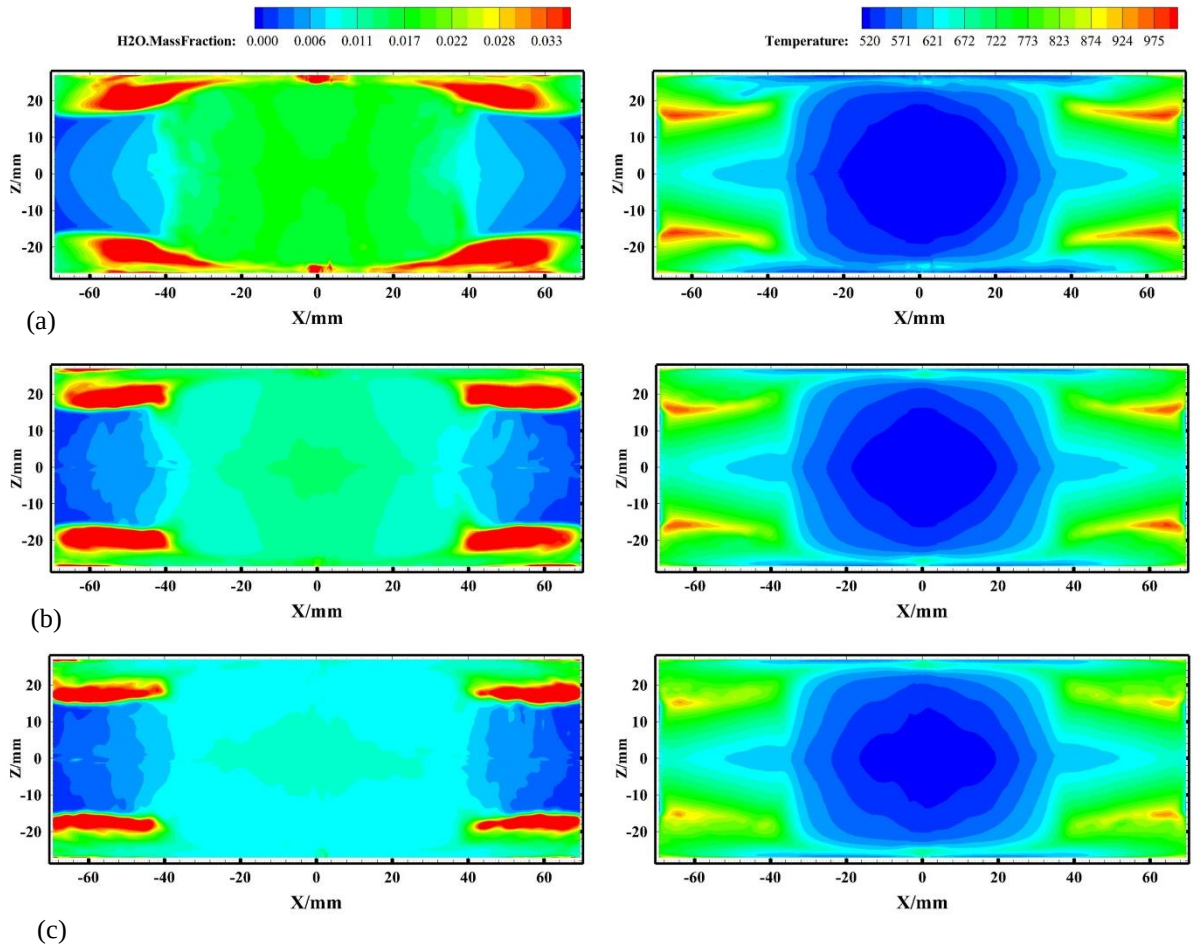


**Fig. 17 The influence of water mist humidification on the time-averaged water vapor content and temperature on the impinging wall: (a) Water mist to air ratio (moist, air) = 5%, (b) Water mist to air ratio (moist, air) = 7.5%, (c) Water mist to air ratio (moist, air) = 10%**

Figure 17 presents the time-averaged water vapor content and temperature distributions on the impinging wall under different humidification conditions when the Reynolds number is ReD=35200. From the water vapor content distribution, it can be observed that when $-20 < X < 20$, the water mist humidification increases from 5% to 10%, nearly doubling the water vapor content on the impinging wall in that region. In the range of $-60 < X < -40$ (or $40 < X < 60$), the water vapor content profile on the wall significantly increases with the increase in humidification. This is because the secondary jet generated after the impingement of the oscillating jet has minimal influence on this region. At higher Reynolds numbers, within the range of $-40 < X < 40$, most of the droplets near the side walls are carried by the airflow to the downstream region of the wall. Therefore, as the humidification increases, the water vapor content in the downstream region of the wall rapidly increases. In the exit region of the wall ($X < -40$ or $X > 40$) and within the range of $-15 < Z < 15$, the lower water vapor content on the wall is due to the formation of a recirculation flow in the confined space after the impingement of the jet, which carries the droplets to the front and back walls. As a result, the limited number of droplets in this region restricts the evaporation of water vapor. The temperature distribution shows that within the range of $-20 < X < 20$, the temperature on the impinging wall decreases with increasing water mist humidification. However, increasing the humidification does not significantly cool the high-temperature region on the wall.

## 4. CONCLUSION

The study used the Eulerian-Lagrangian two-phase flow model to analyze how Reynolds number, droplet diameter, humidification capacity, and impingement distance affect the heat transfer effectiveness of the impingement wall. The main conclusions can be summarized as follows:

- Comparing the temperature changes of impingement walls with and without mist-air, researchers found that beyond a certain threshold, the temperature at the impingement center no longer decreases with an increase in Reynolds number. For instance, at ReD = 20,000, using mist-air impingement resulted in 7.1% lower time-averaged temperature on the axial centerline compared to using dry air. These findings suggest that mist/air impingement cooling is more effective at lower Reynolds numbers.
- As the droplet diameter decreases within the sweeping region, the temperature on the axial centerline increases. A decrease in the droplet diameter from 20μm to 10μm leads to a 2.0% increase in the average temperature of the axial centerline. However, downstream of the impingement wall, smaller

diameter droplets did not significantly improve heat transfer.

- This study also examined the influence of humidification capacity on the impingement wall's heat transfer performance. The results indicate that as the humidification capacity increases from 0 to 5.0, 7.5, and 10%, the temperature drop at the impingement center also increases by 8.5, 12.8, and 18.8%, respectively. Conversely, a lower humidification capacity decreased heat transfer in the downstream region of the impingement wall.
- Regarding impingement distance, the effectiveness of the phase change cooling effect of the droplets is at its best when they hit the center for H/D = 3. However, when X > 8, the heat transfer effect decreases rapidly for H/D = 3. For H/D = 5, phase change cooling resulted in an 8.0% decrease in temperature at the center of impingement. On the other hand, for H/D = 8, mist-air phase change cooling caused a 5.0% reduction in temperature at the impingement center.

The presented findings provide valuable insights into the design and optimization of cooling systems that use impinging mist-air jets. These insights are particularly relevant for low Reynolds numbers, smaller droplet diameters, and higher humidification capacities. The study's results can be of great use to professionals in the field seeking to improve the efficiency and effectiveness of their cooling systems.

## ACKNOWLEDGEMENTS

The authors acknowledge the State Key Laboratory of Long-life High-Temperature Materials (DEC8300CG202210279EE280285) and the Fundamental Research Funds for the Central Universities (501XTCX2023146001) and the Research Fund for International Scientists of National Natural Science Foundation of China (Grant No. 52350410459) and the financial support from the Excellent Postdoctoral Program of Jiangsu Province.

## CONFLICT OF INTEREST

The authors declare that they have no known competing financial interests or personal relationships that could have appeared to influence the work reported in this paper.

## AUTHORS CONTRIBUTION

**W. He**: Conceptualization, Software development, data curation, and visualization aspects. **A. Adam**: Analysis, writing and editing the original draft. **P. Su**: Conceptualization, and manuscript revision. **H. An**: Software implementation, validation, and data curation. **D. Han**: Supervision and funding acquisition roles. **C. Wang**: Editing and review processes.

## REFERENCES

Agricola, L., Hossain, M. A., Ameri, A., Gregory, J. W., & Bons, J. P. (2018). Turbine vane leading edge impingement cooling with a sweeping jet. *ASME Turbo Expo: Turbomachinery Technical Conference and Exposition*. https://doi.org/https://doi.org/10.1115/GT2018-77073

AIAA. (2000). *Miniature fluidic oscillators for flow and noise control - transitioning from macro to micro fluidics.* Fluids 2000 Conference And Exhibit. https://doi.org/https://doi.org/10.2514/6.2000-2554.

Ansys, Inc. (2020). *ANSYS CFX-Solver Theory Guide Release 2020-R1*. http://www.ansys.com

Camci, C., & Herr, F. (2002). Forced convection heat transfer enhancement using a self-oscillating impinging planar jet. *Journal of Heat Transfer Transaction ASME, 124* (4), 770–782. https://doi.org/https://doi.org/10.1115/1.1471521

Cerretelli, C., & Kirtley, K. (2009). Boundary layer separation control with fluidic oscillators. https://doi.org/10.1115/GT2006-90738

Chu, Y. M., Nazeer, M., Khan, M. I., Ali, W., Zafar, Z., Kadry, S., & Abdelmalek, Z. (2020). Entropy analysis in the Rabinowitsch fluid model through inclined Wavy Channel: Constant and variable properties. *International Communications in Heat and Mass Transfer*, *119*, 104980. https://doi.org/10.1016/j.icheatmasstransfer.2020.104980

Hossain, M. A., Agricola, L., Ameri, A., Gregory, J. W., & Bons, J. P. (2018a). Effects of curvature on the performance of sweeping jet impingement heat transfer. *J In 2018 AIAA aerospace sciences meeting (p. 0243).* https://doi.org/10.2514/6.2018-0243

Hossain, M. A., Prenter, R., Lundgreen, R. K., Ameri, A., Gregory, J. W., & Bons, J. P. (2018b). Experimental and numerical investigation of sweeping jet film cooling. *Journal of Turbomachinery*, *140*(3), 031009. https://doi.org/10.1115/1.4038690

Khan, M. I., & Alzahrani, F. (2020). Transportation of heat through Cattaneo-Christov heat flux model in non-Newtonian fluid subject to internal resistance of particles. *Applied Mathematics and Mechanics*, *41*, 1157-1166. https://doi.org/10.1007/s10483-020-2641-9

Khan, M. I., Qayyum, S., Kadry, S., Khan, W. A., & Abbas, S. Z. (2020). Theoretical investigations of entropy optimization in electro-magneto nonlinear mixed convective second order slip flow. *Journal of Magnetics*, *25*(1), 8-14. https://doi.org/10.4283/JMAG.2020.25.1.008

Usman, Khan, M. I., Shah, F., Khan, S. U., Ghaffari, A., & Chu, Y. M. (2022). Heat and mass transfer analysis for bioconvective flow of Eyring Powell nanofluid over a Riga surface with nonlinear thermal features. *Numerical Methods for Partial Differential Equations*, *38*(4), 777-793. https://doi.org/10.1002/num.22696

Kim, S. H., Kim, H. D., & Kim, K. C. (2019). Measurement of two-dimensional heat transfer and flow characteristics of an impinging sweeping jet. *International Journal of Heat and Mass Transfer, 136*, 415–426. https://doi.org/https://doi.org/10.1016/j.ijheatmasstransfer.2019.03.021

Li, X., Gaddis, J. L., & Wang, T. (2001). Mist/steam heat transfer in confined slot jet impingement. Journal of Turbomachinery, *123* (1), 161–167. https://doi.org/https://doi.org/10.1115/1.1331536

Li, X., Gaddis, J. L., & Wang, T. (2003). Mist/steam cooling by a row of impinging jets. *International Journal of Heat and Mass Transfer, 46* (12), 2279–2290. https://doi.org/https://doi.org/10.1016/S0017-9310(02)00521-5

Lundgreen, R. K., Hossain, M. A., Prenter, R., Bons, J. P., Gregory, J., & Ameri, A. (2017). *Impingement heat transfer characteristics of a sweeping jet.* 55th Aiaa Aerospace Sciences Meeting. https://doi.org/10.2514/6.2017-1535.

Menter, F. (1993, July). *Zonal two equation kw turbulence models for aerodynamic flows.* 23rd Fluid Dynamics, Plasmadynamics, and Lasers Conference (p. 2906). https://doi.org/10.2514/6.1993-2906

Park, T., Kara, K., & Kim, D. (2018). Flow structure and heat transfer of a sweeping jet impinging on a flat wall. *International Journal of Heat and Mass Transfer, 124*, 920–928. https://doi.org/https://doi.org/10.1016/j.ijheatmasstransfer.2018.04.016

Peng, J., Hong-yan, H., Guo-tai, F., & Zhong-qi, W. (2009). Numerically simulating mist/steam impingement cooling with phase change. *Journal of Harbin Engineering University, 30* (10), 1097–1101. https://doi.org/10.3969/j.issn.1006-7043.2009.10.003

Schlichting, H., & Gersten, K. (1979). *Boundary-layer theory.* Springer. https://doi.org/https://doi.org/10.1007/978-3-662-52919-5

Song, Y. Q., Khan, M. I., Qayyum, S., Gowda, R. P., Kumar, R. N., Prasannakumara, B. C., ... & Chu, Y. M. (2021). Physical impact of thermo-diffusion and diffusion-thermo on Marangoni convective flow of hybrid nanofluid (MnZiFe2O4–NiZnFe2O4–H2O) with nonlinear heat source/sink and radiative heat flux. *Modern Physics Letters B, 35*(22), 2141006. https://doi.org/10.1142/S0217984921410062

Tan, X. M., Li, Y. F., & Zhang, J. Z. (2013). Numerical simulation of mist/air cooling in a single slot jet impingement. *Journal of Aerospace Power, 28* (1), 129–135. https://api.semanticscholar.org/CorpusID:138265390

Thurman, D., Poinsatte, P., Ameri, A., Culley, D., Raghu, S., & Shyam, V. (2015). *Investigation of spiral and sweeping holes.* ASME Turbo Expo: Turbine Technical Conference and Exposition. https://doi.org/10.1115/1.4032839

Wang, T., & Dhanasekaran, T. S. (2010). Calibration of a computational model to predict mist/steam impinging jets cooling with an application to gas turbine blades. Journal of Heat Transfer, *132* (12), https://doi.org/https://doi.org/10.1115/1.4002394

Wang, T., Gaddis, J. L., & Li, X. C. (2005). Mist/steam heat transfer of multiple rows of impinging jets. International *Journal of Heat and Mass Transfer, 48* (25-26), 5179–5191. https://doi.org/https://doi.org/10.1016/j.ijheatmasstransfer.2005.07.016

Weigand, B., & Spring, S. (2011). Multiple jet impingement- a review. *Heat Transfer Research, 42* (2), 101–142. https://doi.org/10.1615/HeatTransRes.v42.i2.30

Zhou, J., Wang, X., Li, J., & Lu, H. (2017). Cfd analysis of mist/air film cooling on a flat plate with different hole types. *Numerical Heat Transfer, Part A: Applications, 71* (11), 1123–1140. https://doi.org/https://doi.org/10.1080/10407782.2017.1337994

Zhou, W. W., Yuan, L., Liu, Y. Z., Peng, D., & Wen, X. (2019). Heat transfer of a sweeping jet impinging at narrow spacings. *Experimental Thermal and Fluid Science, 103*, 89–98. https://doi.org/https://doi.org/10.1016/j.expthermflusci.2019.01.007